International Journal of Naval Architecture and Ocean Engineering 11 (2019) 750–764

Contents lists available at ScienceDirect

International Journal of Naval Architecture and Ocean Engineering

journal homepage: http://www.journals.elsevier.com/international-journal-of-naval-architecture-and-ocean-engineering/

URANS prediction of hydrodynamic interaction between LHD and supply vessel during replenishment in calm water

Qin Yao Wong, Haoli Tang, Yuting Jin*, Jonathan Duffy, Shuhong Chai, Christopher Chin

National Centre for Maritime Engineering and Hydrodynamics, Australian Maritime College, University of Tasmania, Locked Bag 1395, Launceston, TAS, 7250, Australia

ARTICLE INFO

Article history:
Received 10 November 2018
Received in revised form
7 March 2019
Accepted 21 March 2019
Available online 23 March 2019

1. Introduction

Replenishment at Sea (RAS) is used extensively for transferring fuel and supplies while two ships are underway. It is crucial for naval vessels that require prolonged endurance while minimising the weight of the vessels. It eliminates the need of returning to ports for refilling. When the ships are to manoeuvre adjacent to each other towards the same direction at constant speed, hydrodynamic forces will form in between the ships due to the close proximity and thus affect the manoeuvring capability of the vessels. The ships may experience a force which attracts them towards or repels them away from each other. This increases the risk of collision or capsize if care is not taken during the operation. Therefore, it is important to investigate ship to ship interactions in order to develop an applicable solution for safe operations.

Model testing has been used to obtain data for mathematical models to predict ship to ship interactions. For example, Vantorre et al. (2002) developed a numerical model for ship to ship hydrodynamic interactions during overtaking and adjacent manoeuvres for large ships. It is suggested that further improvement of the model required extensive experimental data. Lataire et al. (2009) investigated ship to ship interactions during lightering operations using model tests and offered results as benchmark data for validation purposes. Lataire et al. (2011) attempted to derive a mathematical model for solving lightering operation with the model established by Vantorre et al. (2002). However, the model developed was found to possess discrepancy in yaw moment. Therefore, Lataire et al. (2012) utilised the data provided by Lataire et al. (2009) and proposed an improved empirical model for ship to ship interactions during lightering manoeuvres.

Different methodologies are available for the numerical simulations of ship to ship interactions. Jiankang et al. (2001) studied the effect of two ships advancing in shallow water on the generated wave interaction by developing a wave equation model with moving surface pressure and utilising Galerkin finite element method for dynamic pressure and free surface elevations on the hull. Skejic et al. (2009) used a two-time scale model which combined a seakeeping and manoeuvring model to predict ship to ship interactions. Each hydrodynamic interaction is integrated as separate modules to prevent interference between the modules. Fonfach et al. (2011) studied the interaction with or without wavemaking for both perfect and viscous fluid models to determine the importance of including free surface effect.

With the rapid growth in computational power in the past decade, the viscous Reynolds-Averaged Navier Stokes (RANS) based Computational Fluid Dynamics (CFD) analysis has drawn much attention due to its suitability in describing three-dimensional turbulent flows as discussed by Chen et al. (2003). They used RANS method based on Chimera grids to investigate the ship to ship interactions in shallow waterways with lateral restrictions. Zou and Larsson (2013) also utilise RANS method to predict the ship to ship interaction during lightering operations in shallow water. Similarly, Sadat-Hosseini et al. (2011) studied the interactions between two tankers in shallow water using the URANS simulation with focus on small under-keel clearance. Although it was found that URANS underestimated the motions of the ships in calm water by an average of 33%, the method is considered dependable in modelling ship to ship interaction as it possesses the smallest error values compared to various potential flow-based methods (Mousaviraad et al., 2016b).

The use of Computational Fluid Dynamics (CFD) gained popularity in recent years due to its high accuracy and lower cost required compared to model testing. Similar to mathematical models, CFD requires benchmark data from experiments to validate the results. Mousaviraad et al. (2016a) conducted an

* Corresponding author.
E-mail address: Yuting.jin@utas.edu.au (Y. Jin).
Peer review under responsibility of Society of Naval Architects of Korea.

https://doi.org/10.1016/j.ijnaoe.2019.03.004

Nomenclature

B_{OA}	Beam overall (m)
β	Drift angle (degrees)
h	Water depth (m)
Fr	Froude number
Fr_{LHD}	Froude number based on LHD length
Fr_{SV}	Froude number based on SV length
K	Roll moment (N.m)
K'	Non-dimensional roll moment
LCG	Longitudinal centre of gravity (m)
L_{OA}	Length overall (m)
L_{PP}	Length between perpendiculars (m)
n	Propeller rate (rpm)
N	Yaw moment (N.m)
N'	Non-dimensional yaw moment
T	Draft (m)
U	Velocity/Flow speed (m/s)
Δx	Relative longitudinal position between CGs
X	Surge force (N)
X'	Non-dimensional surge force
Δy	Relative transverse position between CGs
Y	Sway force (N)
Y'	Non-dimensional sway force

Abbreviation

CFD	Computational fluid dynamics
LHD	Landing helicopter dock
RAS	Replenishment at sea
SV	Supply vessel
URANS	Unsteady Reynolds Averaged Navier-Stokes
VOF	Volume of fluid

experimental analysis of ship to ship interactions and the results are used to validate the unsteady Reynolds Averaged Navier-Stokes (URANS) simulations which are carried out by Mousaviraad et al. (2016b). It was found that repelling sway forces and roll away moments are induced on both vessels due to the increased pressure at the sides of the ships adjacent to each other through the experiment. The results are mirrored by the URANS prediction of the interactions.

The wake region created during ship advancing is one of the important factors in affecting the hydrodynamic interactions during RAS. Yuan et al. (2016) investigated this wake effect by placing the ship in and out of the wake region of the other ship using a 3-D Rankine source method developed by Yuan et al. (2015) for ship to ship interactions in shallow water. Moreover, Jin et al. (2016) investigated ship to ship interactions at model and full scales and found scale effect affected the surge force significantly. Model scale should only be used as an indication for determining the trend of results at full scale as variances are found in boundary layer, flow separation, vortex formation and wave breaking at the aft body (Hochkirch and Mallol, 2013). The presence of free surface and effect of wall boundary conditions have significant influence on the accuracy of the simulation (Chen et al., 2003).

To date, the majority of RANS-based simulation on ship to ship interaction has been conducted at very low Froude numbers and thus the free surface effects are neglected. However, the waves generated by ships at relatively high Froude number can radiate at a great distance and affect nearby ships, as waves contain energy that must be dissipated to surrounding fluid. Based on the importance of accurately modelling the wake and free surface URANS computations are presented in the present paper on ship to ship interaction during Replenishment at Sea (RAS) between a LHD and a SV in calm deep-water conditions. To validate the current numerical modelling technique, computations are compared to benchmark cases from literature. Additionally, the predicted surge force on a single ship is compared with experimental data. The validated numerical model is used to perform a series of systematic computations to provide comprehensive knowledge on ship to ship interactions. Furthermore, the main focus is placed on the influence of relative lateral separations, longitudinal separations and different forward speeds.

2. Ship geometry

The models used for the simulations are a 1:70 scale LHD and SV shown in Fig. 1. The LHD model is fitted with forward and aft bilge keels and is simulated at full-load condition whereas the SV is analysed at minimum operating displacement. The particulars of the models are provided in Table 1.

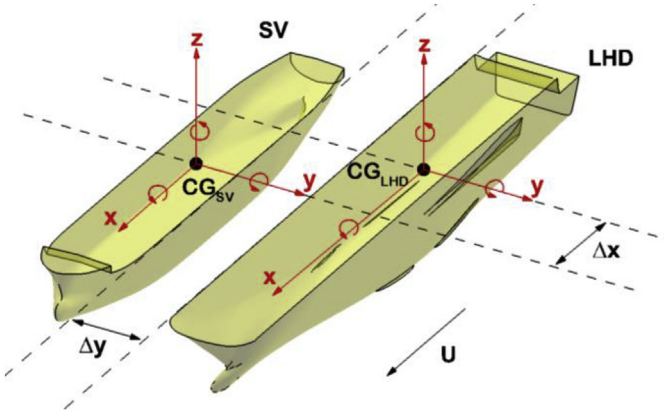

Fig. 1. Coordinate system and configuration of the test setup.

3. Computational method

The present computations are executed using commercial URANS solver STAR-CCM+. Finite volume method is used for resolving incompressible RANS equation in integral form. Hydrodynamic interactions between a SV and a LHD in deep calm water are investigated using time dependent URANS simulations.

Table 1
Principal particulars of LHD and SV.

Particulars	LHD		SV	
	Model Scale	Full Scale	Model Scale	Full Scale
L_{OA} (m)	3.30	230.80	2.73	191.30
B_{OA} (m)	0.43	29.90	0.44	31.00
L_{PP} (m)	2.96	207.20	2.40	168.00
T_{FP} (m)	0.10	7.10	0.10	7.18
T_{AP} (m)	0.10	7.10	0.12	8.38
LCG (m)	1.43	100	1.27	88.58
VCG (m)	0.19	13.51	0.12	8.08
TCG (m)	0.0	0.0	0.0	0.0
Displacement	78.18 kg	27486.00 t	92.90 kg	32662.00 t

3.1. URANS equations and turbulence model

The governing equations for the two phase incompressible flow combining air and water are given by the URANS equations coupled with the conservation of continuity (Rusche, 2003), as shown in Eqs. (1) and (2).

$$\frac{\partial \rho \bar{u}}{\partial t} + \nabla \cdot [\rho \bar{u}\bar{u}] = -\nabla \bar{p} + g \cdot x \nabla \rho + \nabla \cdot [\mu \nabla \bar{u} + \rho \tau] + \sigma_T \kappa_\gamma \nabla_\gamma \quad (1)$$

$$\nabla \cdot \bar{u} = 0 \quad (2)$$

Here, $\overline{u} = (u, v, w)$ is the time-averaged velocity field in Cartesian coordinates, $\overline{p}$ denotes the time-averaged pressure including hydrostatic, $\rho = \rho(x)$ represents the fluid density which varies with the content of air/water in the computational cells, g is the gravitational acceleration, $x = (x, y, z)$ are the Cartesian coordinates, μ is the dynamic molecular viscosity and τ is the Reynolds stress tenor,

$$\tau = \frac{2}{\rho}\mu_t S - \frac{2}{3} kI \quad (3)$$

where μ_t is the dynamic eddy viscosity, k is the turbulent kinetic energy per unit mass and $S = (1/2(\nabla u + (\nabla u)^T))$ is the fluid strain rate tensor. ∇ is the gradient operator $(\partial/\partial x, \partial/\partial y, \partial/\partial z)$. The last term in Eq. (1) represents surface tension, where σ_T is the surface tension coefficient which is 0.074 kg/s^2 between air and water at 20 °C and κ_γ is the surface curvature. The presence of surface tension has insignificant effects in civil engineering applications (Jacobsen et al., 2012). Eqs. (1)–(3) are solved for air and water simultaneously, where the fluids are tracked using the volume of fraction γ. γ is 0 for air and 1 for water, and any intermediate value is a mixture of the two fluids. This is commonly known as the Volume of Fluid (VOF) method. The distribution of γ is modelled by an advection equation:

$$\frac{\partial \gamma}{\partial t} + \nabla [u\gamma] \cdot \nabla \cdot [u_r \gamma (1-\gamma)] = 0 \quad (4)$$

The last term on the left-hand side is a compression term, which limits the smearing of the interface, and u_r is the relative velocity vector. Using γ, the spatial variation in fluid properties, such as ρ and μ, can be derived through weighting:

$$\rho = \gamma \rho_{water} + (1-\gamma)\rho_{air} \quad (5)$$

$$\mu = \gamma \mu_{water} + (1-\gamma)\mu_{air} \quad (6)$$

For the closure of the system, $k-\omega$ shear stress transport (SST) turbulence model as described by Menter (1994) and Wilcox (2008) is utilised, which will resolve both near and far field viscous flow.

3.2. Free surface modelling

The STAR-CCM + software package utilises VOF method for free surface of segregated flows modelling as mentioned previously. Immiscible fluid phases are assumed to share velocity and pressure fields in a control volume and are governed by the same set of equations describing momentum, mass and energy transport in a single-phase flow. Spatial distribution of each phase at individual time steps are attained through solving the transport equations for the phase volume fraction. Ship motion is not modelled in the present computation.

3.3. Computational domain, boundary conditions and grid

The computational domain is generated according to recommendations made by CD-adapco (2016) for virtual towing tank simulations. The fluid domain is modelled to represent seas ambient calm open water. The dimensions of the control volume are selected according to the recommendation made by ITTC (2011) as illustrated in Fig. 2. The boundary condition of velocity inlet is applied at the upstream, side, top and bottom of the domain while

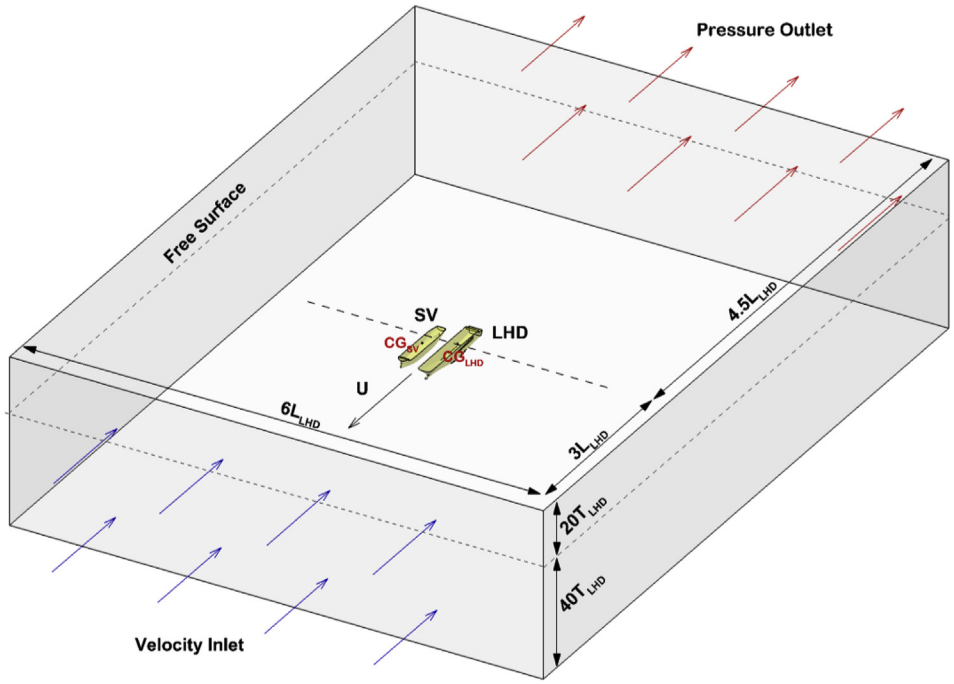

Fig. 2. Boundaries and dimensions of the computational domain.

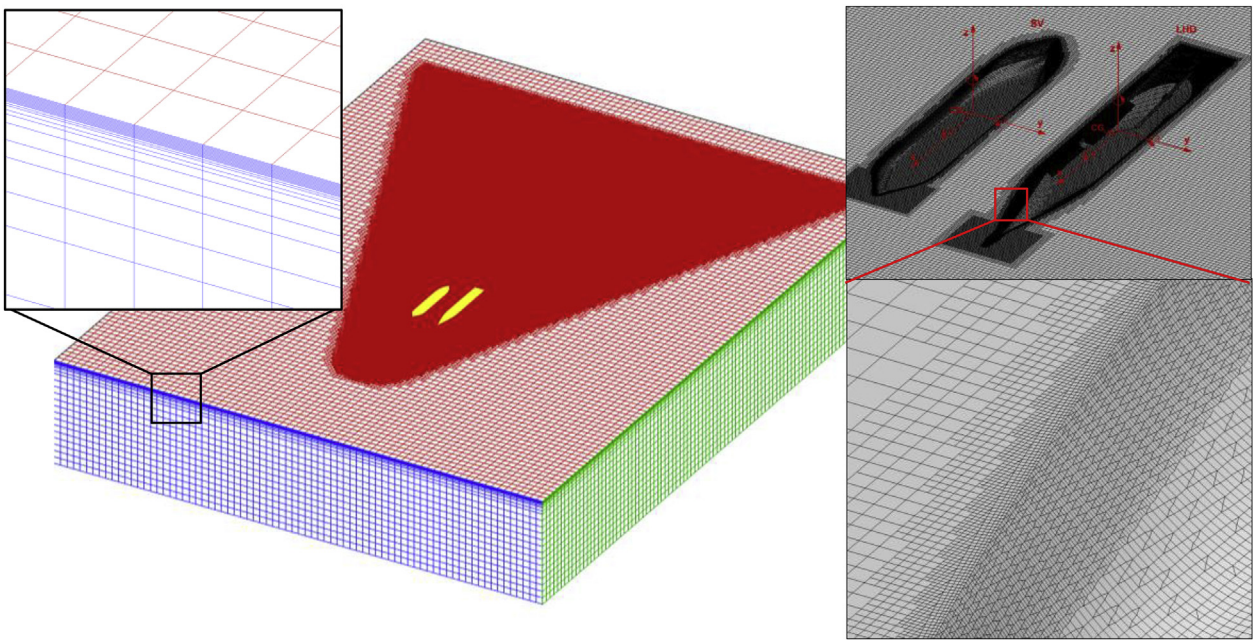

Fig. 3. Illustration of computational grid sliced at free surface.

pressure outlet is used at the downstream. A no-slip wall condition is implemented for the hulls. VOF wave damping is added to cover 4 m from the upstream and downstream of the domain to prevent wave reflection or reversed flow. This setup remains the same for all cases. The ship hulls are constrained in surge, sway, heave, roll, pitch and yaw.

The coordinate system of the simulation is provided in Fig. 1. Illustrations of the grid distribution for both hull and the domain are shown in Fig. 3. Hexahedral trimmer and surface remesher are implemented to generate the unstructured volume mesh with local refinements. A total of approximately 9.7 million cells are generated with base size of 1 m. Anisotropic trimmer refinement in z direction is implemented at free surface for the capture of wave generated by the vessels. Isotropic trimmer refinement is applied to contain the region where Kelvin wake is anticipated. With prism layer mesh and the all y + wall treatment, a y + value between 30 and 50 is maintained along the hulls for resolving the turbulent boundary layer.

4. Validation of numerical method

4.1. Benchmark ship to ship interaction cases

The credibility of the presented computations is demonstrated through replicating benchmark ship to ship interaction cases by Vantorre et al. (2002), where a series of model tests were conducted at Flanders Hydraulic Research (FHR) investigating the hydrodynamic interactions between a KVLCC2 vessel and an Aframax tanker during lightering operations. Two cases are simulated at different water depth to draft ratios as shown in Table 2. Virtual disks are employed to both vessels to produce propeller induced flow at respective propeller rate. Predictions from the present paper are compared to CFD data from Zou and Larsson (2013), Sadat-Hosseini et al. (2011) Jin et al. (2016) and EFD data from FHR, as tabulated in Table 3. Each data set has been designated an abbreviation as follows:

- S: CFD results from the present study – with free surface

Table 2
Benchmark conditions of Tests A and B conducted by Vantorre et al. (2002).

Conditions	Test A	Test B
Depth, h (m)	0.230	0.270
$T_{Aframax}$ (m)	0.100	0.200
$h/T_{Aframax}$	2.300	1.35
$W_{Tank}/B_{Aframax}$	12.5	12.5
T_{KVLCC2} (m)	0.171	0.171
h/T_{KVLCC2}	1.345	1.579
W_{Tank}/B_{KVLCC2}	9.06	9.06
Speed, U (m/s)	0.356	0.297
Δx (m)	0	0
Δy (m)	1.334	1.334
$n_{Aframax}$ (RPM)	588	384
n_{KVLCC2} (RPM)	344	287

- S_C: CFD results from Chalmers University (Zou and Larsson, 2013) – without free surface
- S_I: CFD results University of Iowa (Sadat-Hosseini et al., 2011) – with free surface
- S_A: CFD results from the Australian Maritime College (Jin et al., 2016) – without free surface
- D: Model scale experiment results from FHR (Vantorre et al., 2002) – with free surface

A comparison between the results gathered from different studies is shown in Table 3. For Test A, all the predicted forces and moments for both Aframax and KVLCC2 lie within the range of literature results provided. All of the CFD results display great deviation when compared with experimental results, D. Although the difference of the surge force for Aframax in S and D is below 20%, for KVLCC2 there is a deviation of approximately 60%. In contrary, the predicted sway force of Aframax deviates up to 76% while KVLCC2 corresponds with just less than 2% of difference compared with experimental data. In the case of yaw moment, both vessels deviate greatly with around 400% of difference when compared to D. Although the correlations between the predicted results from the present study and experimental results are relatively poor, they agree well with CFD data from literature.

Table 3
Forces and moments on the Aframax and the KVLCC2.

Test A							
		Aframax	KVLCC2			Aframax	KVLCC2
X	D	−0.77	−3.92	K	D	0	–
(N)	S_C	−1.10	−2.54	(Nm)	S_C	−0.29	0.31
	S_I	−1.32	−2.97		S_I	−0.29	0.35
	S_A	−0.93	−2.35		S_A	−0.28	0.29
	S	**−0.95**	**−2.44**		**S**	**−0.28**	**0.35**
Y	D	0.30	−0.85	N	D	−1.38	−3.44
(N)	S_C	1.41	−1.12	(Nm)	S_C	−0.19	0.88
	S_I	1.51	−1.20		S_I	−0.57	1.33
	S_A	1.32	−0.84		S_A	−0.24	0.80
	S	**1.23**	**−0.86**		**S**	**−0.32**	**0.93**
Test B							
		Aframax	KVLCC2			Aframax	KVLCC2
X	D	−0.37	−1.89	K	D	0.01	–
(N)	S_C	−1.22	−1.84	(Nm)	S_C	−0.08	0.37
	S_I	−1.39	−2.00		S_I	−0.06	0.40
	S_A	−1.08	−1.78		S_A	−0.06	0.38
	S	**−1.07**	**−1.72**		**S**	**−0.08**	**0.32**
Y	D	1.55	−1.41	N	D	−0.19	0.68
(N)	S_C	1.23	−1.29	(Nm)	S_C	−0.09	0.80
	S_I	1.13	−1.42		S_I	−0.21	1.19
	S_A	1.46	−1.30		S_A	−0.35	0.84
	S	**1.50**	**−1.33**		**S**	**−0.42**	**1.14**

Likewise, in Test B, all predicted results for both vessels are within the range of solutions from literature except for yaw moment of Aframax which is 17% greater than the closest results. In terms of surge and sway forces, both vessels show good correlations with a maximum deviation of 4% when compared to results from S_A. When compared to experimental data, Test B exhibits better correlations than Test A. The difference in surge for Aframax yields 66% while KVLCC2 is less than 10%. The predicted sway force for both vessels agree well with D with just less than 7% of deviation. Similarly, the yaw moment for both vessels deviate with a maximum of 55% from experimental results.

It can also be observed from Fig. 4 that the pressure distributions on the ship hulls show similar pattern compared to Zou and Larsson (2013) predictions, even though the free surface was neglected in their computations. In general, the presented computations exhibit reasonable agreement with benchmark EFD and CFD data, and therefore can be adopted for the continuing studies.

4.2. Single ship surge force validation for LHD and SV

In addition to the ship to ship interaction cases with the Aframax and KVLCC2 operating in close proximity presented in the previous section, two sets of data for single ship resistance of LHD and SV are available for validation. Model testing to measure the resistance of the hulls was conducted in the Australian Maritime College towing tank and the obtained results are shown in Table 4. The experiments were conducted with the models constrained in sway, heave, roll, pitch and yaw. Each vessel was towed with speeds of 0.86 m/s and 1.0 m/s, equivalent to 14 and 16 knots full scale respectively. Fig. 5 displays the Experimental Fluid Dynamics (EFD) results with the CFD computations performed with trend lines shown. The results of LHD match well with 0.5% of difference while SV has variance of approximately 6%. Overall, a good agreement has been found between the computed surge force data and experimental data for each ship towed at forward speed without the other ship present.

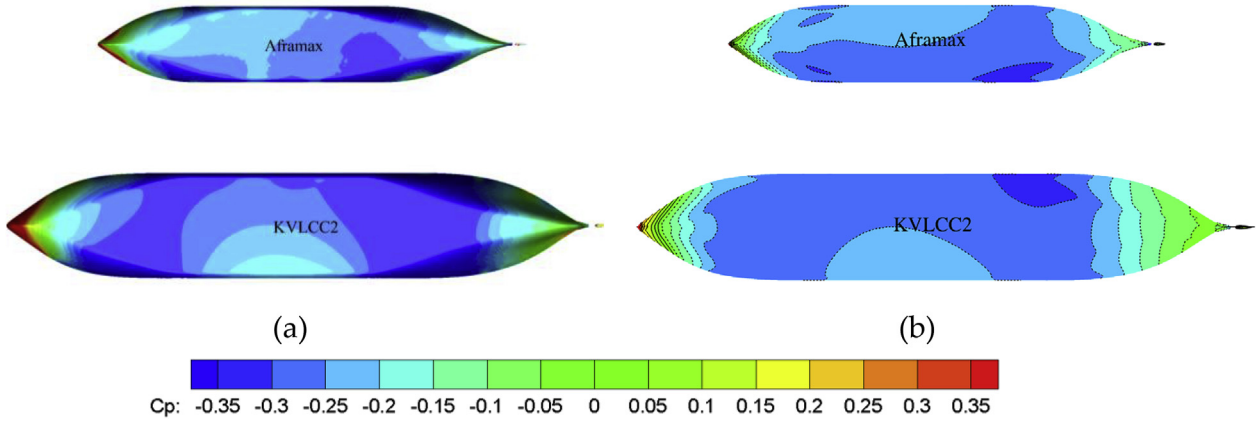

Fig. 4. Comparison of the pressure distribution on the Aframax and KLVCC2 for Test A in top view (a) with free surface modelling, and (b) benchmark case by Zou and Larsson (2013).

Table 4
Surge force validation on the LHD and SV operating independently.

Speed	X(N) LHD		Error (%)	X(N) SV		Error (%)
(m/s)	EFD	CFD		EFD	CFD	
0.61	–	−1.31	–	–	−2.17	–
0.86	−2.45	−2.46	0.27	−3.68	−3.96	7.66
1.00	−3.18	−3.19	0.42	−5.78	−5.5	−4.84
1.23	–	−5.08	–	–	−10.46	–
1.54	–	−7.46	–	–	−24.34	–

5. Systematic computations

Having validated the numerical approach, it will now be used to investigate the hydrodynamic interactions due to RAS operation between LHD and SV in a deep calm water condition. Systematic computations are carried out to investigate the effect of longitudinal separation, lateral distances and advancing speed on both vessels. The investigated longitudinal separation, denoted as Δx, measured from the centre of gravity of both vessels, are −100, −75, −50, −25, 0, 15.5, 46, 58.9, 80 and 112 m in full scale. The lateral separations Δy investigated are 20, 30, 40, 50 and 70 m in full scale. These test conditions are scaled by Froude law of similitude and non-dimensionalised for model scale computation purposes as shown in Table 5. At Δx of 15.5 m and 58.9 m, which is $\Delta x/L_{pp}$ (SV) = 0.09 and 0.35 respectively, the RAS station on SV will align with the two RAS station on LHD. For investigating the influence of longitudinal separation Δx, the lateral separation Δy is fixed at $\Delta y/L_{pp}(SV) = 0.24$, while the effect of varying lateral separation Δy is studied at fixed $\Delta x/L_{pp}(SV) = 0.09$. The speeds are selected based on the typical speed used during RAS operations, which is 16 knots at full scale, in this case 1.0 m/s at model scale. In addition, four different advancing speeds, 10, 14, 20 and 25 knots, are chosen to study the effect of increasing speed with the vessels fixed at $\Delta y/L_{pp}(SV) = 0.24$ and $\Delta x/L_{PP}(SV) = 0.09$. The advancing speed, computed interaction forces and moments are non-dimensionalised using Eqs. (7)–(11).

$$Fr = \frac{U}{\sqrt{gL_{PP}}} \tag{7}$$

$$X' = \frac{X}{0.50.5\rho U^2 TL_{PP}} \tag{8}$$

$$Y' = \frac{Y}{0.50.5\rho U^2 TL_{PP}} \tag{9}$$

$$K' = \frac{K}{0.50.5\rho U^2 TL_{PP}^2} \tag{10}$$

$$N' = \frac{N}{0.50.5\rho U^2 TL_{PP}^2} \tag{11}$$

5.1. Numerical uncertainty analysis

For the systematic computations, the sensitivity of the mesh size and time-step are investigated. The verification process for determining the uncertainties within the simulation are carried out as described by Stern et al. (2001). A verification study is undertaken for evaluating the simulation numerical uncertainty, U_{SN} using grid-spacing uncertainty, U_G and time-step uncertainty, U_T as shown in Eq. (12). The iterative convergence uncertainty is omitted due to its insignificant influence.

$$U_{SN} = \sqrt{U_G^2 + U_T^2} \tag{12}$$

Three different combinations of grids and time-step, which yield the same expansion ratio, r_i, are selected to study convergence behaviour. The grid uncertainty analysis was carried out at the smallest time step while the time step uncertainty analysis was carried out for medium grid. The r_i value chosen, as recommended

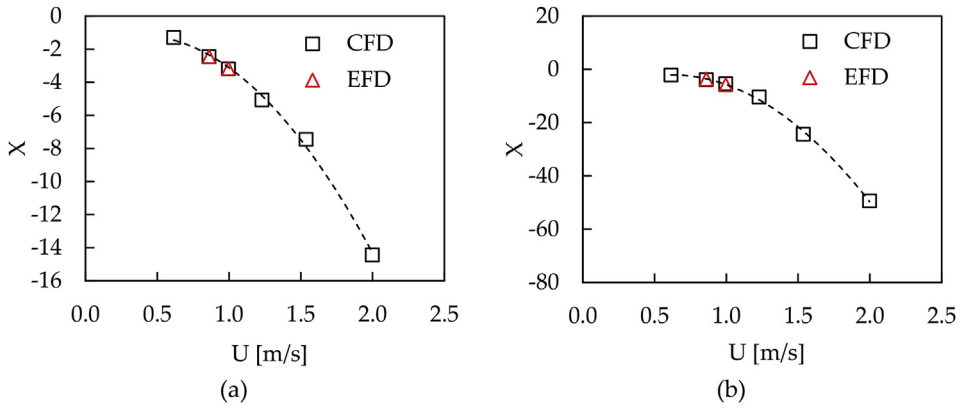

Fig. 5. Comparison of the surge force experienced by the vessel at different speeds (a) LHD and (b) SV.

Table 5
Matrix for the systematic computations.

Speed (m/s)	Fr_{LHD}	Fr_{SV}	$\Delta x/L_{pp}(SV)$	$\Delta y/L_{pp}(SV)$
0.61	0.113	0.126	0.09	0.24
0.86	0.160	0.177	−0.60, −0.45, −0.30, −0.15, 0.0, 0.09, 0.27, 0.35, 0.48, 0.67	0.12, 0.18, 0.24, 0.30, 0.42
1.00	0.186	0.206	0.09	0.24
1.23	0.228	0.253	0.09	0.24
1.54	0.286	0.317	0.09	0.24

Table 6
Number of elements and time-step used for the convergence studies.

	Grid (number of elements)	Time-step (s)
No. 1	9,412,666	0.005
No. 2	3,543,072	0.01
No. 3	1,273,950	0.02

by ITTC (2008), is $\sqrt{2}$ for the grid study and 2 for the time-step study. The differences between the three solutions, $\varepsilon_{32} = S_3 - S_2$ and $\varepsilon_{21} = S_2 - S_1$ are used to determine the convergence ratio, $R_i = \varepsilon_{21}/\varepsilon_{32}$. Depending on the value of R_i, three conditions are possible: i) $0 < R_i < 1$, monotonic convergence, ii) $R_i < 0$, oscillatory convergence and iii) $1 < R_i$, monotonic divergence. The total number of grids and time-steps used for the convergence studies are given in Table 6. Results for grid and time-step uncertainties are tabulated in Table 7 and Table 8. For the grid uncertainty analysis, both sway force and yaw moment possess higher uncertainties compared to surge force and roll moment. Similarly, it is found that the simulation is less dependent on time-step as the uncertainties are all below 6%. The calculated U_{SN} as shown in Table 9 are below 15% which is within an acceptable range, thus demonstrating the feasibility of undertaking further systematic computations.

5.2. Influence of longitudinal separation

The influence of the longitudinal separation, Δx, is investigated with the lateral distance fixed at $\Delta y/L_{pp}(SV) = 0.24$. The resulting hydrodynamic forces and moments imposed on the vessels for varying longitudinal separations are shown in Fig. 6. To further investigate the scenario the predicted free surface elevation is shown in Fig. 7 and the pressure distribution around the vessels is presented in Figs. 8 and 9.

From Fig. 6, when $\Delta x/L_{pp}(SV)$ is between −0.6 and −0.3, both vessels experience similar magnitude of non-dimensionalised surge force X′ as shown in Fig. 6(a). Compared to the single vessel configuration this indicates an increase of X′ on the LHD and a decrease of X′ on the SV because from the single ship resistance simulations performed, the SV experiences greater resistance than the LHD. When $\Delta x/L_{pp}(SV) > -0.3$, X′ on the SV increases and reaches a maximum value at $\Delta x/L_{pp}(SV) = 0.3$, after which the force reduces. Conversely, the X′ experienced by the LHD decreases and reaches a minimum at 0.3. A low pressure region, about −100Pa, is created by the divergent wave of the LHD forward of LCG on SV as shown in Fig. 9 (a) and (b) producing a forward surge force which therefore reduces X′ on the SV. The highest X′ on both vessels occurs when the Kelvin wake of one vessel causes a lower pressure region aft of the LCG on the other vessel thus creating more surge force for that vessel. Similarly, the lowest X' is seen when low pressure region created is forward of the LCG.

The non-dimensionalised sway forces Y′ in Fig. 6(b) are acting in the opposite direction with SV having a slightly higher magnitude overall. The highest Y′ for both vessels occur when $\Delta x/L_{pp}(SV) = 0$. Both vessels experience a sway force towards each other for $\Delta x/L_{pp}(SV)$ between −0.4 and 0.4 which are Fig. 7 (c) to Fig. 7 (h). In these positions, the interference of the wave created by the bows as seen in Fig. 7, causes the pressure in between both vessels to reduce. This is illustrated in Figs. 8 and 9 at which low pressure regions can be seen on the starboard side of the LHD and port side of the SV. When interference of wave is not apparent, the vessels experience repulsive forces. Y' increases as the distance diminishes and decreases as the distance gets larger. When $\Delta x/L_{pp}(SV) > 0.4$

Table 7
Grid uncertainty analysis results.

Variable	r_G	Solutions			R_G	Convergence	$\delta^*_{RE}G$ (%S_1)	U_G (%S_1)
		S_1	S_2	S_3				
X'_{LHD}	$\sqrt{2}$	-2.04×10^{-2}	-2.10×10^{-2}	-2.18×10^{-2}	0.740	Monotonic	8.61	−1.30
Y'_{LHD}	$\sqrt{2}$	-2.83×10^{-3}	-3.13×10^{-3}	-2.68×10^{-3}	−0.657	Oscillatory	–	−8.01
K'_{LHD}	$\sqrt{2}$	-4.71×10^{-5}	-5.13×10^{-5}	-4.46×10^{-5}	−0.621	Oscillatory	–	−7.04
N'_{LHD}	$\sqrt{2}$	-1.49×10^{-4}	-1.33×10^{-4}	-1.05×10^{-4}	0.536	Monotonic	−11.91	−12.98
X'_{SV}	$\sqrt{2}$	-2.65×10^{-2}	-2.73×10^{-2}	-2.86×10^{-2}	0.592	Monotonic	4.42	−2.93
Y'_{SV}	$\sqrt{2}$	3.74×10^{-3}	3.73×10^{-3}	4.62×10^{-3}	−0.017	Oscillatory	–	11.87
K'_{SV}	$\sqrt{2}$	-1.99×10^{-4}	-2.09×10^{-4}	-1.95×10^{-4}	−0.621	Oscillatory	–	−3.42
N'_{SV}	$\sqrt{2}$	-8.10×10^{-4}	-8.01×10^{-4}	-9.84×10^{-4}	−0.052	Oscillatory	–	−11.33

Table 8
Time-step uncertainty analysis results.

Variable	r_T	Solutions			R_T	Convergence	$\delta^*_{RE}T$ (%S_1)	U_T (%S_1)
		S_1	S_2	S_3				
X'_{LHD}	2	-2.04×10^{-2}	-2.04×10^{-2}	-2.03×10^{-2}	0.667	Monotonic	−0.27	−0.13
Y'_{LHD}	2	-2.86×10^{-3}	-2.83×10^{-3}	-2.80×10^{-3}	0.800	Monotonic	−3.79	−2.84
K'_{LHD}	2	-4.62×10^{-5}	-4.71×10^{-5}	-4.83×10^{-5}	0.800	Monotonic	7.92	−5.94
N'_{LHD}	2	-1.56×10^{-4}	-1.49×10^{-4}	-1.62×10^{-4}	−0.500	Oscillatory	–	−4.41
X'_{SV}	2	-2.64×10^{-2}	-2.65×10^{-2}	-2.66×10^{-2}	0.398	Monotonic	0.13	−0.07
Y'_{SV}	2	3.76×10^{-3}	3.74×10^{-3}	3.78×10^{-3}	−0.571	Oscillatory	–	0.42
K'_{SV}	2	-2.00×10^{-4}	-1.99×10^{-4}	-1.97×10^{-4}	0.579	Monotonic	−0.72	−1.11
N'_{SV}	2	-7.52×10^{-4}	-8.10×10^{-4}	-7.46×10^{-4}	−0.904	Oscillatory	–	−4.25

Table 9
Numerical uncertainty of the computation.

Variable	U_{SN}(%CFD)
X'_{LHD}	1.31
Y'_{LHD}	8.50
K'_{LHD}	9.21
N'_{LHD}	13.71
X'_{SV}	2.93
Y'_{SV}	11.88
K'_{SV}	3.60
N'_{SV}	12.10

both vessels experience forces in opposite direction. The higher pressure regions caused by the free surface elevation as shown in Fig. 8 (e) and (f) impose a positive sway force on LHD.

The measured non-dimensionalised roll moment K' is found to be insignificant in magnitude compared to other forces and moments. It is discovered that the Kelvin wake of one vessel changes the instantaneous wetted surface area for the other vessel and therefore becomes a major factor in generating roll moment. Pressure differences are created causing the hull to generate a roll moment. The SV experiences negative roll moment as displayed in Fig. 6(c), indicating roll to port, for $\Delta x/L_{pp}(SV)$ between −0.4 and 0.4. As seen in Fig. 9, the low pressure region near the free surface on the port side imposes a negative roll moment on the SV. The LHD experiences a roll moment towards the SV at negative Δx. For positive Δx LHD experiences negative roll moment that reduces in magnitude gradually. Although lower pressure occurs on the starboard side of the hull, consistent higher pressure regions near the free surface caused by the wave (as seen in Fig. 8) generate an outward roll moment. This phenomenon is not seen on the SV as its hullform generates greater wake therefore results in greater influence on LHD.

The trend in the non-dimensionalised yaw moments is similar for the LHD and SV, as displayed in Fig. 6(d). When the SV is behind the LHD, both vessels experience a positive yaw moment, which pushes the bow of the SV and stern of the LHD towards each other. The yaw moment starts to decrease when $\Delta x/L_{pp}(SV)$ has been increased to −0.3. Once $\Delta x/L_{pp}(SV)$ becomes positive, the yaw moment for both vessels become negative and increase in magnitude. Similarly, when $\Delta x/L_{pp}(SV)$ is more than 0.3, the yaw moment reduces on both vessels. The longitudinal and lateral separation influences how the Kelvin wave pattern from one vessel influences the other. When the waves created by the SV interacts with the hull of LHD aft of its LCG as shown in Fig. 7, a lower pressure region is created causing a pressure difference between port and starboard sides of LHD in Fig. 8. Therefore, the stern of LHD is pushed inwards resulting in a positive yaw moment. After the wave pattern generated by the SV interacts with the LHD ahead of its LCG, the pressure at this location becomes lower as shown in Fig. 8 and thus induces a negative yaw moment, which brings LHD bow-in towards the SV. The SV behaves in the same manner which is influenced by the Kelvin wave pattern of the LHD.

At $\Delta x/L_{pp}(SV) = 0.35$ where the RAS station on both vessels will align, the non-dimensional sway force and non-dimensional roll moment for both are found to be minimum while the non-dimensional yaw moment will be at its maximum. A configuration was not tested where all interaction forces and moments were negligible. However, the recommended range of operation based on the smallest surge force, sway force and roll moment is $\Delta x/L_{pp}$

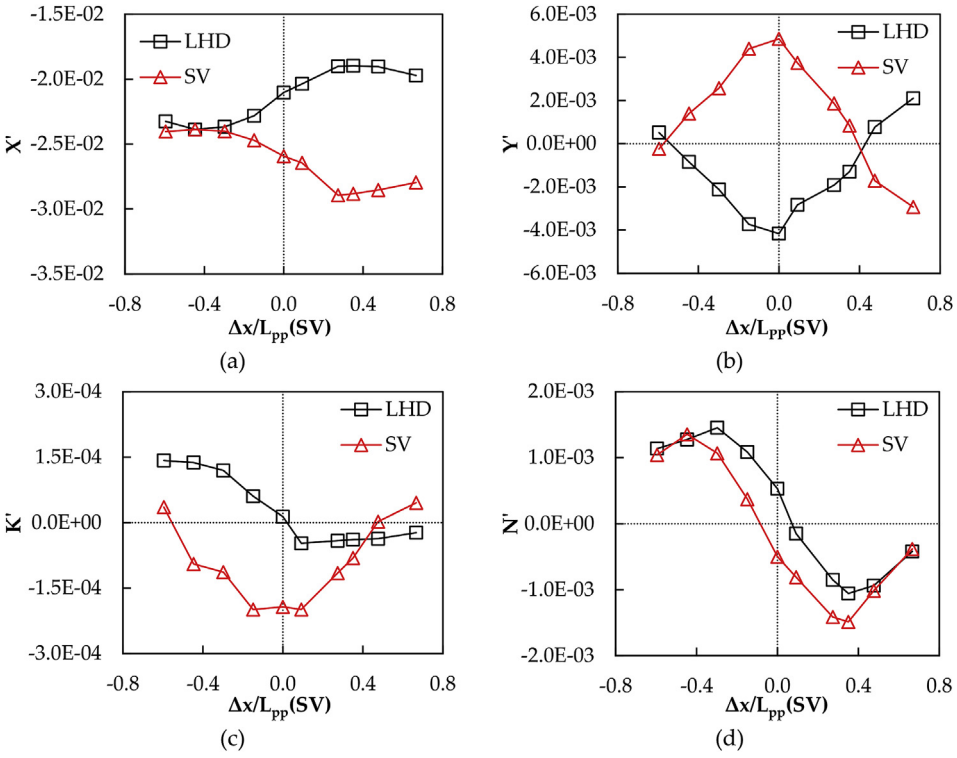

Fig. 6. Interaction forces and moments on the LHD and SV at $Fr_{LHD} = 0.186$, $Fr_{SV} = 0.206$ and varying longitudinal separation, Δx. (a) surge force, (b) sway force, (c) roll moment, and (d) yaw moment.

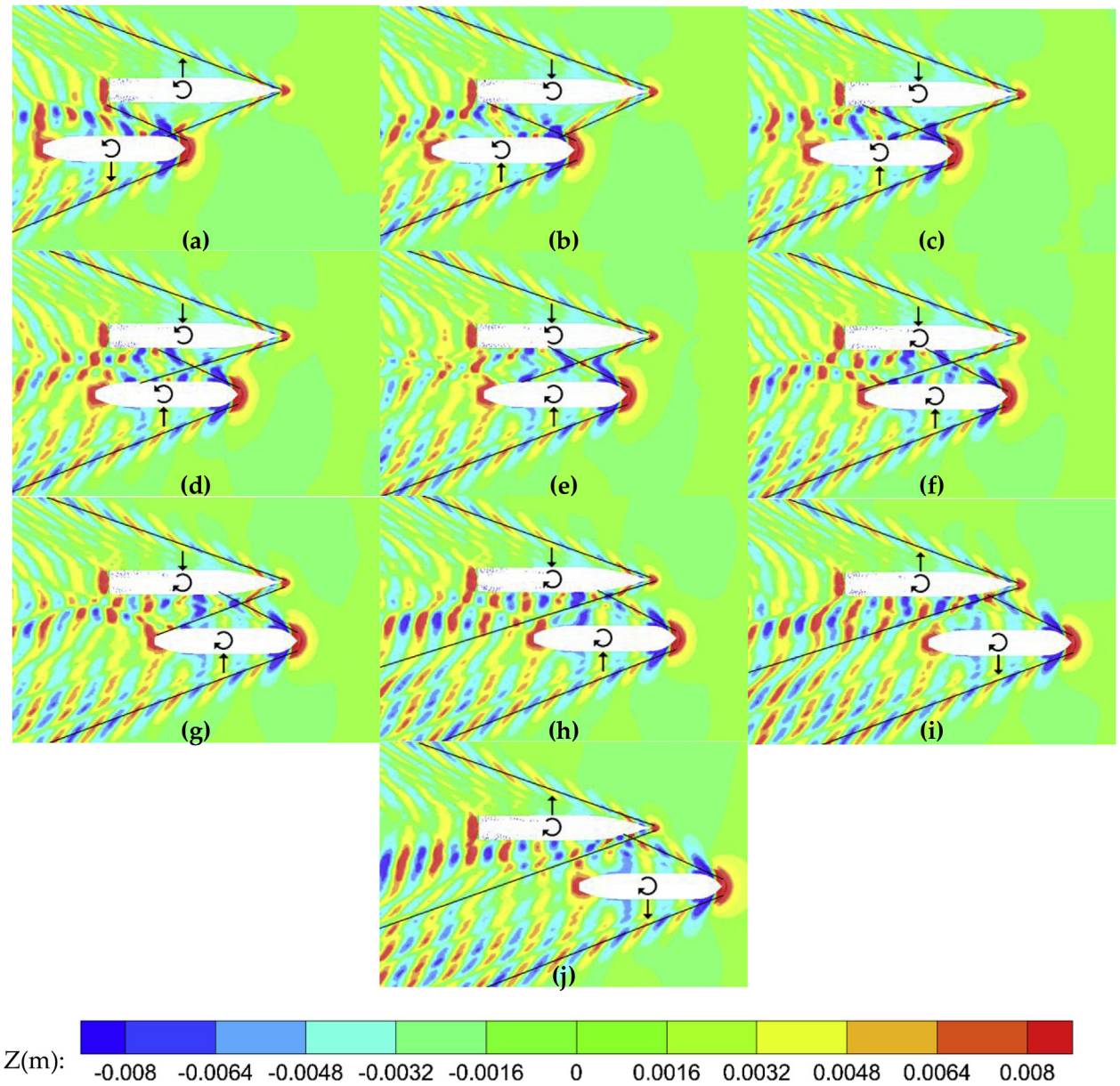

Fig. 7. Predicted free surface elevation at varying longitudinal separation, Δx. (a) $\Delta x/L_{pp}(SV) = -0.60$, (b) $\Delta x/L_{pp}(SV) = -0.45$, (c) $\Delta x/L_{pp}(SV) = -0.30$, (d) $\Delta x/L_{pp}(SV) = -0.15$, (e) $\Delta x/L_{pp}(SV) = 0$, (f) $\Delta x/L_{pp}(SV) = 0.09$, (g) $\Delta x/L_{pp}(SV) = 0.27$, (h) $\Delta x/L_{pp}(SV) = 0.35$, (i) $\Delta x/L_{pp}(SV) = 0.48$ and (j) $\Delta x/L_{pp}(SV) = 0.67$.

(SV) from 0.3 to 0.5. It should be noted that the non-dimensional yaw moment is relatively large for this range of $\Delta x/L_{pp}(SV)$, however this may be countered with rudder deflection.

5.3. Influence of lateral distance

With longitudinal separation fixed at $\Delta x/L_{pp}(SV) = 0.09$, the influence of the lateral separation is investigated, and the resulting hydrodynamic forces and moments imposed on the vessels are presented in Fig. 10. To gain insight into the interaction forces and moments the predicted free surface elevation is given in Fig. 11 and the pressure distribution on each vessel is provided in Figs. 12 and 13.

From Fig. 10(a), it can be deduced that lateral separation has very little influence on the non-dimensional surge force experienced by the vessels undergoing RAS, as it remains relatively constant from $\Delta y/L_{pp}(SV)$ of 0.12–0.42. The trend of the non-dimensional sway force acting on both vessels are in opposite direction with the SV experiencing the largest non-dimensional sway force, as shown in Fig. 10(b). As the lateral separation between the vessels decreases, greater free surface disturbance is seen which creates a low pressure region on the hulls and hence a greater non-dimensional sway force. It can be seen that the pressure variation on the starboard side of the LHD in Fig. 12(a) ($\Delta y/L_{pp}(SV) = 0.12$) is greater than in Fig. 12(e) ($\Delta y/L_{pp}(SV) = 0.42$) and the same can be seen on the port side of SV in Fig. 13.

The non-dimensional roll moment experienced by the LHD marginally increases as the lateral separation is decreased, as shown in Fig. 10(c). This is demonstrated in the pressure distribution on the starboard side of LHD in Fig. 12 where greater surface disturbances are apparent at smaller $\Delta y/L_{pp}(SV)$ thus creating more high pressure regions causing a larger roll-away moment. However, on the SV a counter-intuitive trend is found at $\Delta y/L_{pp}(SV) = 0.12$ and 0.18 where large roll-away moments are seen. In Fig. 11(a) and

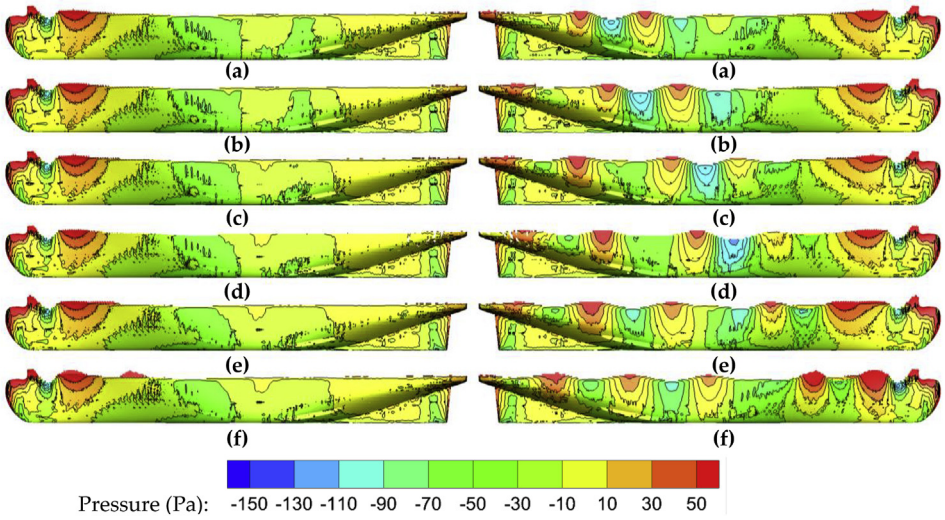

Fig. 8. Predicted pressure distributions on the port (left) and starboard (right) sides of LHD sliced at dynamic free surface for different Δx (vertical scale magnified three times). (a) $\Delta x/L_{pp}(SV) = 0$, (b) $\Delta x/L_{pp}(SV) = 0.09$, (c) $\Delta x/L_{pp}(SV) = 0.27$, (d) $\Delta x/L_{pp}(SV) = 0.35$, (e) $\Delta x/L_{pp}(SV) = 0.48$ and (f) $\Delta x/L_{pp}(SV) = 0.67$.

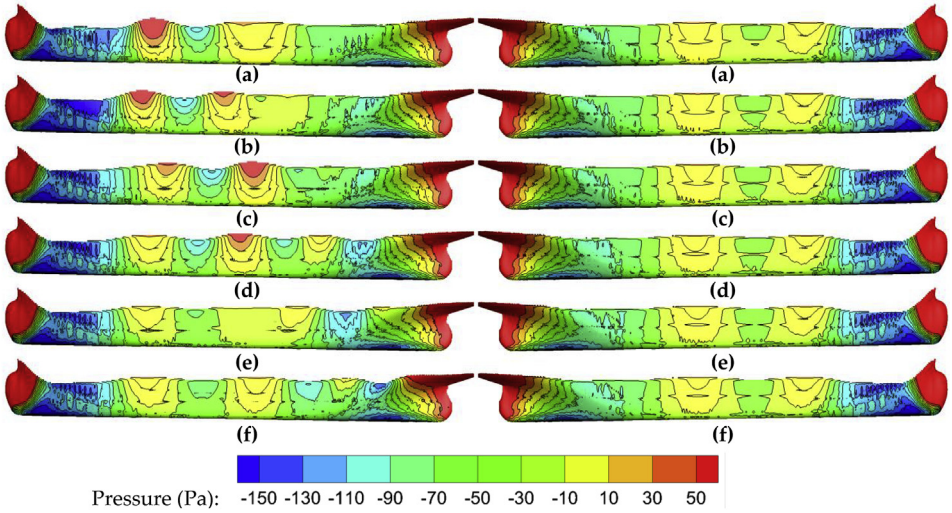

Fig. 9. Predicted pressure distributions on the port (left) and starboard (right) sides of SV sliced at dynamic free surface for different Δx (vertical scale magnified two times). (a) $\Delta x/L_{pp}(SV) = -0.60$, (b) $\Delta x/L_{pp}(SV) = -0.45$, (c) $\Delta x/L_{pp}(SV) = -0.30$, (d) $\Delta x/L_{pp}(SV) = -0.15$, (e) $\Delta x/L_{pp}(SV) = 0$ and (f) $\Delta x/L_{pp}(SV) = 0.09$.

(b), the waves created by both vessels meet and diffract multiple times. After the initial interference, the waves diffract and contact with the vessels which reflect the waves. The reflected waves from both vessels meet and another diffraction occurs. When the gap between both vessels is small, several diffractions of waves will occur, causing more contact with vessels, therefore creating greater roll moment as well as changing the instantaneous wetted surface area of the hull. As seen in Fig. 11(c)–(e), the diffracted waves only contact with the vessels once, resulting in a considerably lower roll-in moment. The non-dimensional roll moment on the LHD is significantly smaller than that on the SV. This can be partly attributed to the LHD being fitted with appendages.

From Fig. 10 (d) it can be seen that $\Delta y/L_{pp}(SV)$ has little influence on the non-dimensional yaw moment experienced by the LHD for the cases tested. However, the magnitude of the non-dimensional yaw moment significantly increases as $\Delta y/L_{pp}(SV)$ decreases. In Fig. 13, it is shown that a low pressure region near the stern of the port side of the SV, which is not seen on the starboard side, generates a negative moment on the vessel. As the lateral separation decreases, the negative pressure becomes larger in magnitude, thus creating greater yaw moment. In contrast, there is no apparent pressure difference near the stern or bow on both side of LHD, therefore the non-dimensional yaw moment is considerably smaller.

At $\Delta y/L_{pp}(SV) = 0.24$, the non-dimensional roll moment of the SV reduces significantly while the non-dimensional sway force and yaw moment exhibit appreciable reduction. All variables except Y' of LHD remain relatively constant at all separations. It can be seen that the interaction forces and moments are generally smaller at $\Delta y/L_{pp}(SV)$ values equal to and greater than 0.24. Hence, such configurations are deemed favourable. Although greater lateral separation will reduce the interaction forces and moments, consideration should be given to the practicalities of conducting RAS for such configurations.

5.4. Influence of forward speed

To determine the influence of forward speed on the interaction

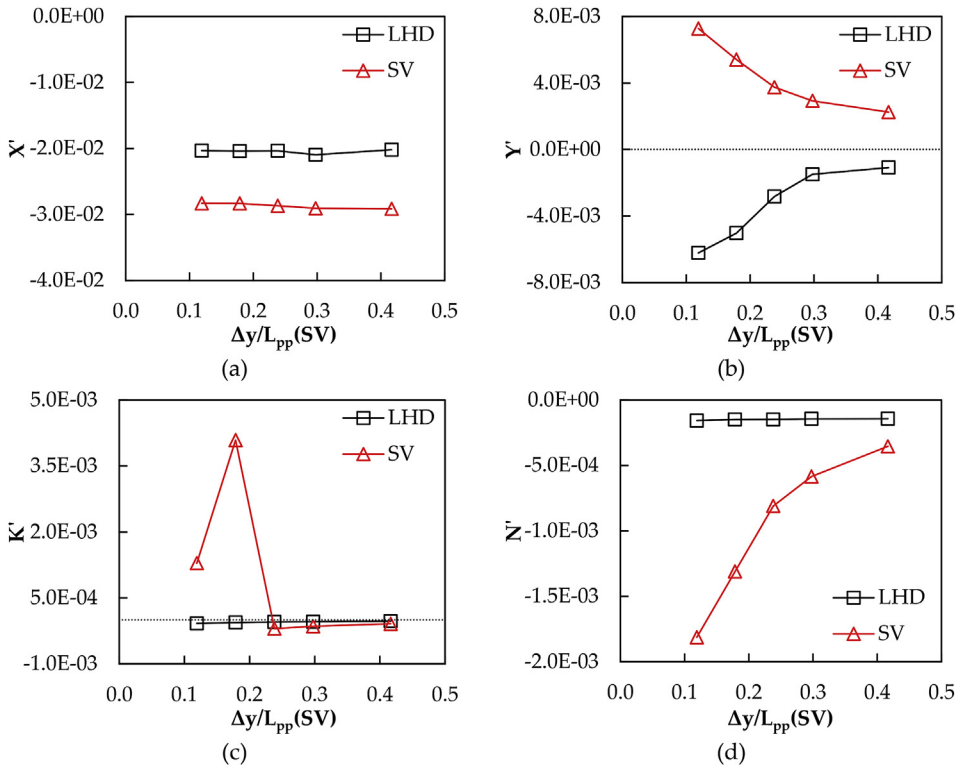

Fig. 10. Interaction forces and moments on the LHD and SV at $Fr_{LHD} = 0.186$, $Fr_{SV} = 0.206$ and varying lateral separation, Δy (a) surge force, (b) sway force, (c) roll moment, and (d) yaw moment.

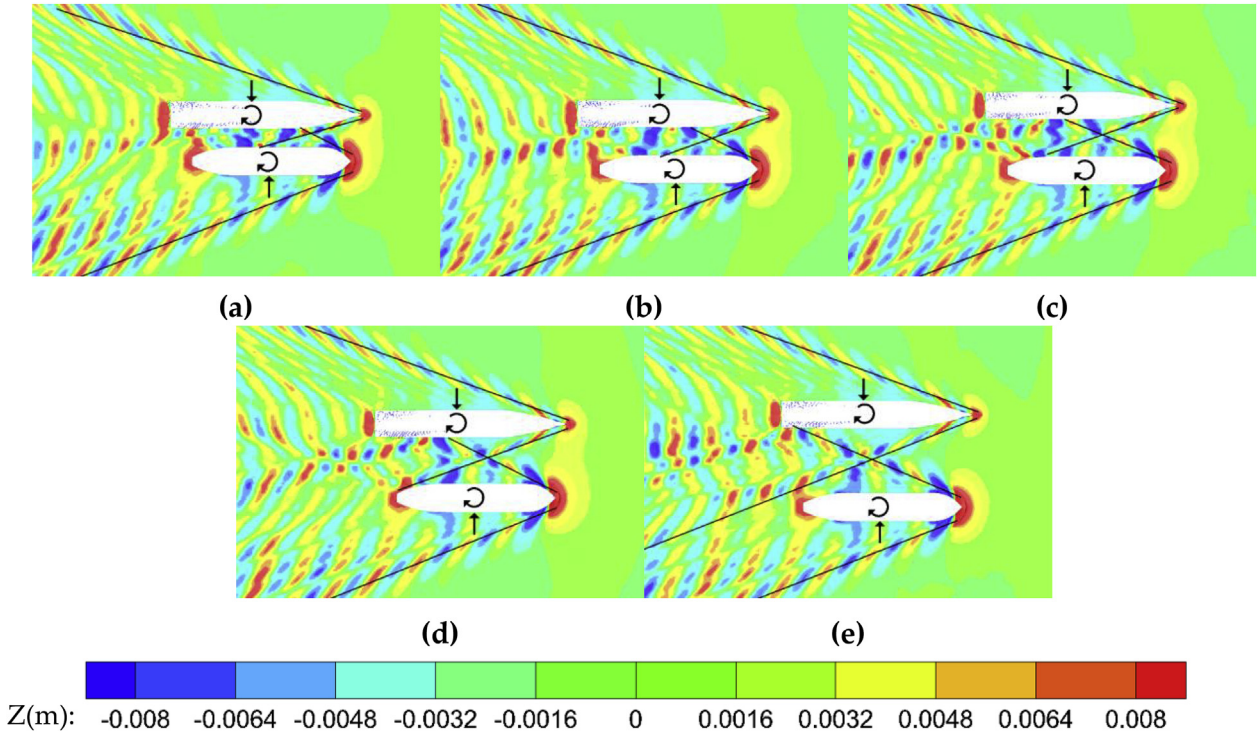

Fig. 11. Predicted free surface elevation of the simulations at varying lateral separation, Δy. (a) $\Delta y/L_{pp}(SV) = 0.12$, (b) $\Delta y/L_{pp}(SV) = 0.18$, (c) $\Delta y/L_{pp}(SV) = 0.24$, (d) $\Delta y/L_{pp}(SV) = 0.30$ and (e) $\Delta y/L_{pp}(SV) = 0.42$.

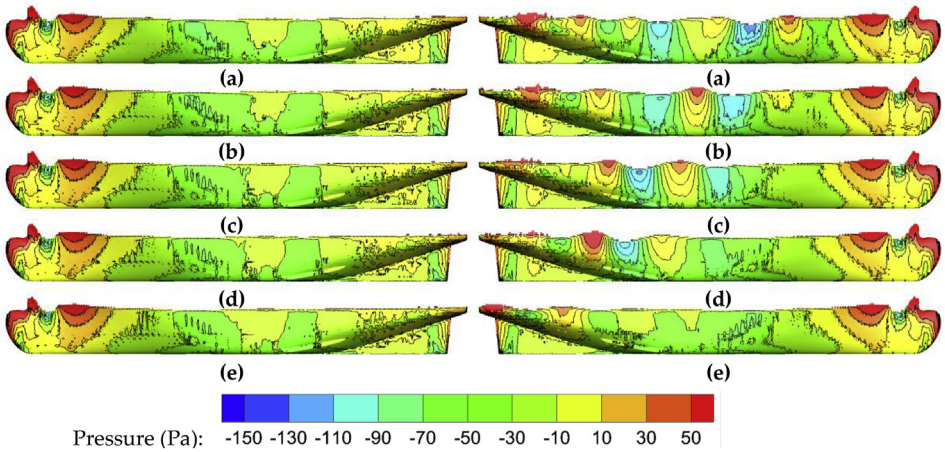

Fig. 12. Predicted pressure distributions on the port (left) and starboard (right) sides of LHD sliced at dynamic free surface for different Δy (vertical scale magnified three times). (a) $\Delta y/L_{pp}(SV) = 0.12$, (b) $\Delta y/L_{pp}(SV) = 0.18$, (c) $\Delta y/L_{pp}(SV) = 0.24$, (d) $\Delta y/L_{pp}(SV) = 0.30$ and (e) $\Delta y/L_{pp}(SV) = 0.42$.

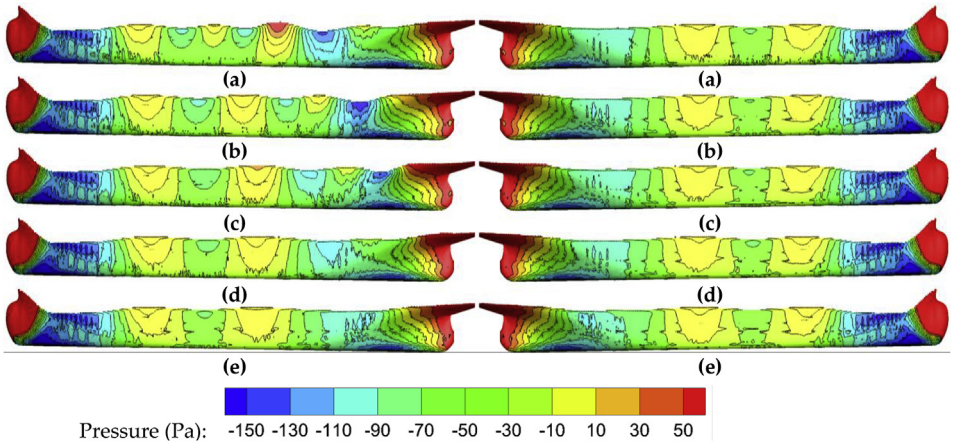

Fig. 13. Predicted pressure distributions on the port (left) and starboard (right) sides of SV sliced at dynamic free surface for different Δy (vertical scale magnified two times). (a) $\Delta y/L_{pp}(SV) = 0.12$, (b) $\Delta y/L_{pp}(SV) = 0.18$, (c) $\Delta y/L_{pp}(SV) = 0.24$, (d) $\Delta y/L_{pp}(SV) = 0.30$ and (e) $\Delta y/L_{pp}(SV) = 0.42$.

hydrodynamic forces and moments experienced, the vessels are constrained at a lateral separation of $\Delta y/L_{pp}(SV) = 0.24$ and lateral separation $\Delta x/L_{pp}(SV) = 0.09$. The resultant forces and moments imposed on the vessels at different constant forward speeds, which is non-dimensionalised as Froude number, are displayed in Fig. 14. The non-dimensional surge force on both vessels increases as Fr becomes greater. The non-dimensional surge force is significantly greater for the SV at high Fr. For the non-dimensional sway force, both vessels experience an attractive sway force as stated previously in section 5.2 and 5.3. However, the LHD is pushed away from the SV when $Fr_{LHD} > 0.228$. This is due to the large divergent wave created by the SV that interacts with the LHD near its LCG as shown in Fig. 15(e), which creates high pressure regions on the starboard side of the LHD around midships and stern sections as shown in Fig. 16(e). The SV is unaffected because the divergent wave of the LHD is considerably smaller in magnitude.

Both non-dimensional roll moment and yaw moment are found to be relatively insignificant due to the chosen separations as discussed in previous sections. When $0.113 < Fr_{LHD} < 0.228$, both vessels encounter negative roll moment which causes them to roll to port. This is caused by the low pressure regions presented on starboard side of LHD in Fig. 16 and port side of SV in Fig. 17. However, when $Fr_{LHD} > 0.228$, the LHD starts to roll to starboard. Similarly, this is caused by the divergent wave of SV creating high pressure region on the starboard side of the LHD and near its LCG in Fig. 16(e) thus creating a roll moment inwards. The non-dimensional yaw moment experienced by both vessels is negative indicating the bow of LHD and stern of SV are being rotated towards each other. This moment on the LHD is induced by the bow wave generated by the SV which has its trough situated near the bow of the LHD and the crest is imposed on the stern as seen in Fig. 15. Similarly, the bow wave of the LHD creates a low pressure region on the port side aft body of the SV in Fig. 17, therefore causing the stern to yaw inwards. At $Fr_{LHD} = 0.286$, the magnitude of the non-dimensional yaw moment decreases. From the free surface elevation around the SV in Fig. 15, the vessel reaches its hull speed with the wave troughs located at bow and stern, and therefore the non-dimensional yaw moment experienced by the vessel is diminished. As can be seen in Fig. 17, although the pressure magnitude is higher in (e), the difference in pressure on both sides of the hull in (f) is greater than in (e). While for the LHD in Fig. 15(e), the pressure differences are greater in size, however in (f) the pressure regions are greater in quantity, therefore in both cases yield similar N'.

Due to the high wake making ability of the SV at high operating speeds, the RAS operation speed should be limited to a maximum

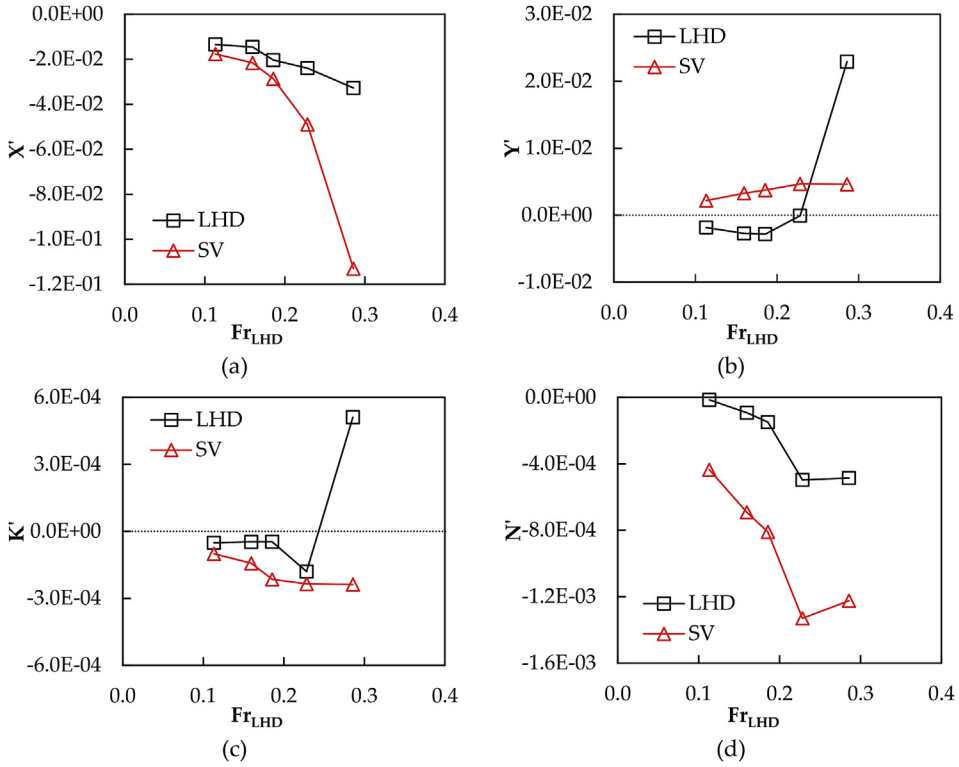

Fig. 14. Predicted interaction forces and moments on the LHD and SV at respective Fr_{LHD}. (a) surge force, (b) sway force, (c) roll moment, and (d) yaw moment.

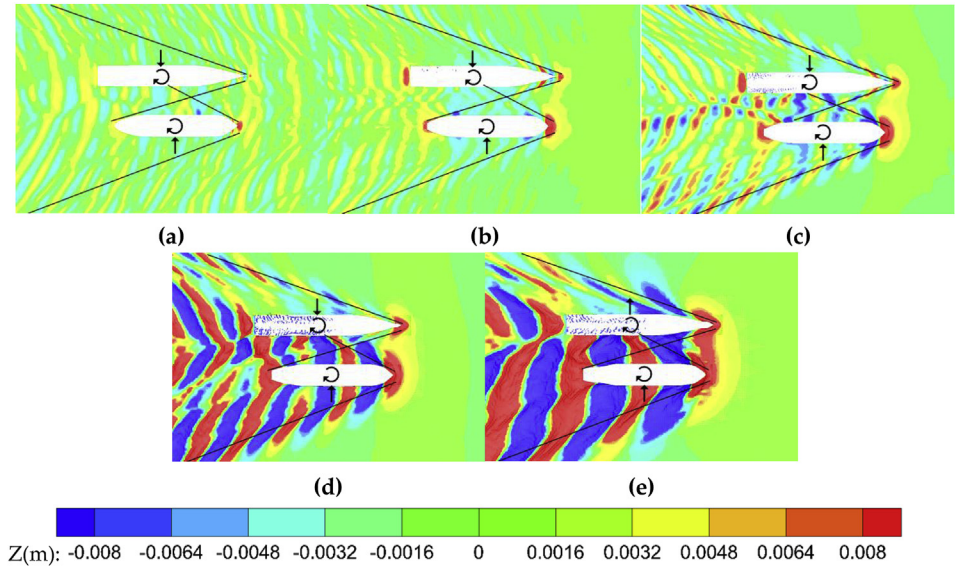

Fig. 15. Predicted free surface elevation of the simulations at varying forwarding speed, U (a) $Fr_{LHD} = 0.113$, $Fr_{SV} = 0.126$, (b) $Fr_{LHD} = 0.160$, $Fr_{SV} = 0.177$, (c) $Fr_{LHD} = 0.186$, $Fr_{SV} = 0.206$, (d) $Fr_{LHD} = 0.228$, $Fr_{SV} = 0.253$ and (e) $Fr_{LHD} = 0.286$, $Fr_{SV} = 0.317$.

of $Fr_{LHD} = 0.186$ which is 1 m/s in model scale and equivalent to 16 knots in full scale.

6. Concluding remarks

This paper investigates and discusses the influence of longitudinal separation, lateral separation and different constant forward speeds on the hydrodynamic interactions between a LHD and a supply vessel during RAS operations. Validation of the computations is performed against benchmark studies on the Aframax and KVLCC2. It is found that the predicted results show good correlation with computed data from literature. The predicted pressure distribution on the hull is also shown to be similar to the provided benchmark results. In addition, the predicted resistance of each ship without the other present shows good correlation with physical scale model testing results. The variances in results are considered to be within acceptable limits, thus the feasibility of the presented computational setup is demonstrated.

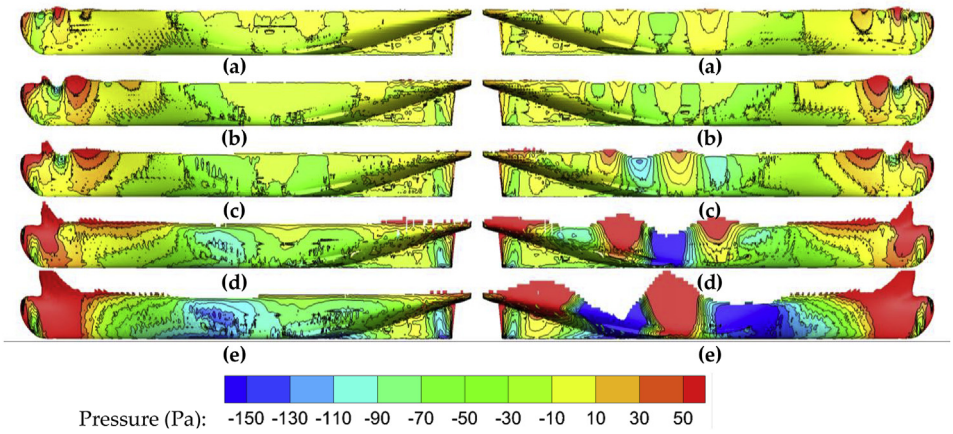

Fig. 16. Predicted pressure distributions on the port (left) and starboard (right) sides of LHD sliced at dynamic free surface for different U (vertical scale magnified two times). (a) $Fr_{LHD} = 0.113$, $Fr_{SV} = 0.126$, (b) $Fr_{LHD} = 0.160$, $Fr_{SV} = 0.177$, (c) $Fr_{LHD} = 0.186$, $Fr_{SV} = 0.206$, (d) $Fr_{LHD} = 0.228$, $Fr_{SV} = 0.253$ and (e) $Fr_{LHD} = 0.286$, $Fr_{SV} = 0.317$.

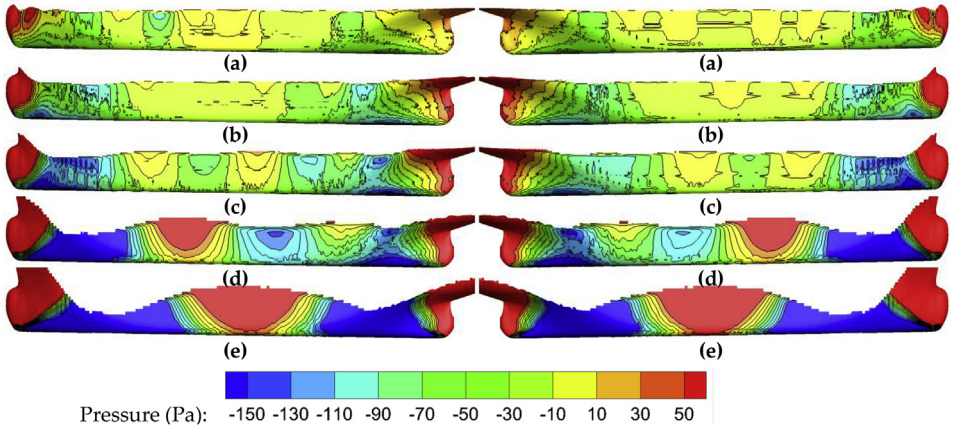

Fig. 17. Predicted pressure distributions below free surface on the port (left) and starboard (right) sides of SV sliced at dynamic free surface for different U (vertical scale magnified two times). (a) $Fr_{LHD} = 0.113$, $Fr_{SV} = 0.126$, (b) $Fr_{LHD} = 0.160$, $Fr_{SV} = 0.177$, (c) $Fr_{LHD} = 0.186$, $Fr_{SV} = 0.206$, (d) $Fr_{LHD} = 0.228$, $Fr_{SV} = 0.253$ and (e) $Fr_{LHD} = 0.286$, $Fr_{SV} = 0.317$.

Systematic computations are carried out to investigate the influence of longitudinal separation, lateral separation and different constant speeds on the LHD and SV during RAS operation. The free surface elevation and pressure distribution on the hulls during hydrodynamic interaction are presented. It is shown that the position of the vessel with respect to the wave field of the other vessel is critical for the hydrodynamic interaction forces and moments on the vessel. From the study (constant lateral separation and varying longitudinal separation), the following is observed:

- When the SV LCG is aft of the LHD LCG, the LHD experiences an increase in non-dimensional surge force. The value reduces and reaches a minimum when the SV LCG is forward of the LHD LCG. Similarly, the SV experiences smaller non-dimensional surge force when the SV LCG is aft of the LHD LCG and its maximum value is reached when the vessel is ahead of the LHD.
- The non-dimensional sway force is the largest for both vessels when their LCGs are adjacent and decreases when the vessels move away from each other in the longitudinal direction.
- Both the LHD and the SV experience non-dimensional yaw moment in the same direction, except when the LCGs are adjacent where the yaw moment on the LHD is bow-away and bow-towards for the SV.

From the study (constant longitudinal separation and varying lateral separation), it is found that:

- All the forces experienced by LHD except for non-dimensional sway force remain relatively unaffected by changing the lateral separation.
- Decreasing the lateral separation has little influence on the non-dimensional surge force experienced by both vessels.
- Non-dimensional sway force is greatest at small lateral separation. A greater free surface disturbance is observed at the smaller lateral separations.
- The SV experiences a large roll moment at small lateral separations due to interference of waves created by both vessels. A large decrease in non-dimensionalised roll moment occurs as lateral separation increases.
- The non-dimensional yaw moment experienced by the SV is found to be greater than that experienced by the LHD due to the pressure difference near the stern and bow.

Through investigation of different constant forward speeds, it observed that:

- At Fr_{LHD} between 0.2 and 0.3 the LHD experiences a sway force away from the SV, where for lower Fr_{LHD} conditions, the LHD moves towards the SV.

- The non-dimensional sway force and roll moment on the SV remains relatively unaffected as Fr_{LHD} increases due to the insignificant size of Kelvin wake generated by LHD unable to create considerable changes to the port side of SV.
- The non-dimensional roll moment experienced by the LHD changes direction at $Fr_{LHD} = 0.286$ due to the large Kelvin wake produced by the SV.
- Non-dimensional yaw moment increases up to $Fr_{LHD} = 0.286$ for both vessels due to greater pressure differences.

Based on where the interaction forces and moments are smallest, a suitable range of operation for RAS by the LHD and SV is recommended to be between $\Delta x/L_{pp}(SV)$ of 0.3–0.5 and $\Delta y/L_{pp}(SV)$ of more than 0.24. With these suggested separations, the maximum forward speed is advised to be 1 m/s (model scale) which is equivalent to 16 knots in full scale. Future work with the inclusion of ship motions and regular waves will provide a better understanding and a more realistic representation of the hydrodynamic interactions. Full scale simulation is also recommended in order to predict the influence of scale effect.

Acknowledgements

This project was conducted as part of a collaborative research agreement with DST Group. Special thanks to the following DST Group staff for their contribution to the project: Jenny Mathew, Daniel Sgarioto and Terry Turner. The authors acknowledge the scholarship support provided by the Australian Maritime College, University of Tasmania on the present work. Computations were performed on the Katabatic and Vortex clusters funded by the Tasmanian Partnership for Advanced Computing (TPAC) program.

References

CD-adapco, 2016. STAR-CCM+: User Guide. NY.

Chen, H.C., Lin, W.M., Liut, D.A., Hwang, W.Y., 2003. An advanced viscous flow computation method for ship-ship dynamic interactions in shallow and restricted waterway. In: Paper Presented at the Proceedings of the International Conference on Marine Simulation and Ship Maneuverability (MARSIM'03). Kanazawa, Japan.

Fonfach, J.M.A., Sutulo, S., Guedes Soares, C., 2011. Numerical study of ship-to-ship interaction forces on the basis of various flow models. In: Paper Presented at the 2nd International Conference on Ship Manoeuvering in Shallow and Confined Water: Ship to Ship Interactions 2011, May 18, 2011 - May 20, 2011, Trondheim, Norway.

Hochkirch, K., Mallol, B., 2013. On the importance of full-scale cfd simulations for ships.. In: Paper Presented at the Proceedings of the 12th International Conference on Computer Applications and Information Technology in the Maritime Industries. Cortona, Italy.

ITTC, 2008. Uncertainty analysis in CFD verification and validation. In: Paper Presented at the 25th International Towing Tank Conference, Fukuoka.

ITTC, 2011. Practical guidelines for ship CFD applications. In: Paper presented at the 26th International Towing Tank Conference, Rio de Janeiro.

Jacobsen, N.G., Fuhrman, D.R., Fredsøe, J., 2012. A wave generation toolbox for the open-source CFD library: OpenFoam. Int. J. Numer. Methods Fluids 70 (9), 1073–1088. https://doi.org/10.1002/fld.2726.

Jiankang, W., Lee, T.S., Shu, C., 2001. Numerical study of wave interaction generated by two ships moving parallely in shallow water. Comput. Methods Appl. Mech. Eng. 190 (15–17), 2099–2110. https://doi.org/10.1016/S0045-7825(00)00223-1.

Jin, Y., Chai, S., Duffy, J., Chin, C., Bose, N., Templeton, C., 2016. RANS prediction of FLNG-LNG hydrodynamic interactions in steady current. Appl. Ocean Res. 60, 141–154. https://doi.org/10.1016/j.apor.2016.09.007.

Lataire, E., Vantorre, M., Delefortrie, G., 2009. Captive model testing for ship to ship operations. In: Paper Presented at the International Conference on Marine Simulation and Ship Maneuverability (MARSIM '09), Panama City, Panama.

Lataire, E., Vantorre, M., Vandenbroucke, J., Eloot, K., 2011. Ship to ship interaction forces during lightering operations. In: Paper Presented at the 2nd International Conference on Ship Manoeuvring in Shallow and Confined Water : Ship to Ship Interaction: Conference Proceedings, London, UK.

Lataire, E., Vantorre, M., Delefortrie, G., Candries, M., 2012. Mathematical modelling of forces acting on ships during lightering operations. Ocean Eng. 55, 101–115. https://doi.org/10.1016/j.oceaneng.2012.07.029.

Menter, F.R., 1994. Two-equation eddy-viscosity turbulence models for engineering applications. AIAA J. 32 (8), 1598–1605. https://doi.org/10.2514/3.12149.

Mousaviraad, S.M., Sadat-Hosseini, S.H., Stern, F., 2016a. Ship–ship interactions in calm water and waves. Part 1: analysis of the experimental data. Ocean Eng. 111, 615–626. https://doi.org/10.1016/j.oceaneng.2015.10.035.

Mousaviraad, S.M., Sadat-Hosseini, S.H., Carrica, P.M., Stern, F., 2016b. Ship–Ship interactions in calm water and waves. Part 2: URANS validation in replenishment and overtaking conditions. Ocean Eng. 111, 627–638. https://doi.org/10.1016/j.oceaneng.2015.10.039.

Rusche, H., 2003. Computational Fluid Dynamics of Dispersed Two-phase Flows at High Phase Fractions. University of London, London.

Sadat-Hosseini, H., Wu, P.C., Toda, Y., Carrica, P., Stern, F., 2011. Urans studies of ship-ship interactions in shallow-water. In: Paper Presented at the RINA, Royal Institution of Naval Architects - 2nd International Conference on Ship Manoeuvering in Shallow and Confined Water: Ship to Ship Interactions 2011.

Skejic, R., Breivik, M., Fossen, T.I., Faltinsen, O.M., 2009. Modeling and control of underway replenishment operations in calm water. In: Paper Presented at the 8th International IFAC Conference on Manoeuvring and Control of Marine Craft, MCMC 2009, September 16, 2009 - September 18, 2009, Guaruja (SP), Brazil.

Stern, F., Wilson, R.V., Coleman, H.W., Paterson, E.G., 2001. Comprehensive approach to verification and validation of CFD simulations—Part 1: methodology and procedures. J. Fluids Eng. 123 (4), 793–802. https://doi.org/10.1115/1.1412235.

Vantorre, M., Verzhbitskaya, E., Laforce, E., 2002. Model test based formulations of ship–ship interaction forces. Ship Technol. Res. 49, 124–141.

Wilcox, D.C., 2008. Formulation of the k-w turbulence model revisited. AIAA J. 46 (11), 2823–2838. https://doi.org/10.2514/1.36541.

Yuan, Z.-M., Ji, C.-Y., Incecik, A., Zhao, W., Day, A., 2016. Theoretical and numerical estimation of ship-to-ship hydrodynamic interaction effects. Ocean Eng. 121, 239–253. https://doi.org/10.1016/j.oceaneng.2016.05.032.

Yuan, Z.-M., Incecik, A., Dai, S., Alexander, D., Ji, C.-Y., Zhang, X., 2015. Hydrodynamic interactions between two ships travelling or stationary in shallow waters. Ocean Eng. 108, 620–635. https://doi.org/10.1016/j.oceaneng.2015.08.058.

Zou, L., Larsson, L., 2013. Numerical predictions of ship-to-ship interaction in shallow water. Ocean Eng. 72, 386–402. https://doi.org/10.1016/j.oceaneng.2013.06.015.